Journal of
Nanoelectronics and Optoelectronics
Vol. 15, pp. 1–8, 2020
www.aspbs.com/jno

ARTICLE

MoO_3/CNTs Loading in Separator for Performance-Improving Current-Collector-Free Lithium Ion Batteries

Peng Peng, Jiewei Chen, Kai Niu, Zhuohai Liu, Hao Huang, Yupeng Zheng, Lehao Liu, Lihua Chu, and Meicheng Li*

A novel strategy for structural design of current-collector-free lithium ion batteries (LIBs) has been proposed, MoO_3/CNTs loading on the single side of a separator by a simple spin-coating method. LIBs with such a MoO_3-based composite separator eliminate the need for metal current collectors and exhibit an extra high specific capacity (0.2C, ~1200 mA h g^{-1}). Faster ion transport and lower charge transfer resistance (R_{ct}) of the composite separator were proved compared with the traditional MoO_3-based electrode, which results in the increased special capacity. In addition, the pseudocapacitive effect caused by vacancies and narrow interval in the MoO_3/CNTs materials also contributes to the high specific capacity of the batteries. The highly efficient ion and electron transport ability of the composite separator were proved in this study, and such a novel design strategy would be an alternative for low-cost LIBs.

Keywords: Current-Collector-Free LIBs, Composite Separator, Ion Diffusion Coefficient, Pseudocapacitive Effect, Charge Transfer Resistance.

1. INTRODUCTION

Kinds of energy storage materials and devices have attracted great attention and deserve a great development in recent years [1–5]. Among them, lithium ion batteries (LIBs) provide an attractive landscape since their high energy density, long lifetime cycle, and high operating voltage [6–11]. In recent years, the issue of ion diffusion and charge transport is widely studied and concerned in the LIBs system [12, 13]. Most of the researches focus on the design of electrode materials, such as hierarchical nanostructure [14, 15], porous structure [16–19], hollow structure [15, 20, 21], heterostructure [22, 23], two/one-dimensional nanomaterials [14, 24, 25], materials with defect sites [25, 26] and so on. There is also some other work on electrode design: free-standing electrode [27], composite electrode [28] and layer-graded electrode [29]. Although many attempts were made in terms of material modification, combining electrodes and separator is also an effective strategy to solve this problem.

Although the separator only serves to separate the anode and cathode electrode in a lithium-ion (Li-ion) battery, they are completely immersed in the electrolyte and are also part of the ion transport system. By growing the active materials on the separator, the active materials have better contact with the electrolyte, and that is beneficial to the transport process of Li^+. Meanwhile, the R_{ct} may also be decreased. However, ensuring that the active substances grow only on one side of the separator is a key problem. We came up with the spin-coating method to solve this issue, in which way the active materials attached to a single side of the separator can be realized. During the simple spin-coating process, active materials could have a better dispersion and more active sites can be exposed. It also takes less time to prepare the composite separator by spin-coating than to synthesize the material first and then prepare the electrode.

MoO_3 materials have attracted the attention of many researchers, because of its high capacity and other good properties [30, 31]. As a semiconductor, the conductivity of MoO_3 is not good [32, 33], if it is directly growing on the separator which cannot conduct electricity, it will not show good performance. Carbon nanotubes (CNTs) was

State Key Laboratory of Alternate Electrical Power System with Renewable Energy Sources, North China Electric Power University, Beijing 102206, China

*Author to whom correspondence should be addressed.
Email: mcli@ncepu.edu.cn
Received: 25 August 2019
Accepted: 16 September 2019

selected as a three-dimensional conductive framework to improve the conductivity of MoO_3.

Here, we chose the CNTs to improve its poor conductivity, attached with MoO_3 together on the surface of the separator. The MoO_3-based composite separator was obtained by a simple spin-coating and subsequent calcination process. Taking advantage of the fact that the separator is a part of the ion transport system, we loaded the anode materials to the separator without binder, to improve the ion transfer capacity inside the battery. The LIBs with such a structure design are binder-free and current-collector-free, reflecting the advantages of no adverse effects of binder and low cost [34–36]. Besides, considering the area of the separator is usually larger than the electrode, the load of the active material can be increased without too much thickness of the active material. Moreover, the simple spin-coating process can also help improve the dispersion of materials. Such a composite separator strategy may be an alternative in the structural design of LIBs.

2. EXPERIMENTAL DETAILS

2.1. Synthesis of MoO_3-Based Composite Separator

0.086 g of ammonium molybdate tetrahydrate (Alfa) and 0.03 g CNTs was dissolved in 2 mL deionized water, then treated ultrasonically or stirred for an hour. A moderate amount of the above solution was dropped on the side of the separators (Whatman) by a spin-coating method. The separators after treatment were dried at 50° overnight and then calcinated at 500° for 5 hours under vacuum. Then the MoO_3-based composite separators were obtained. The mass of MoO_3 on the separate was calculated and determined by the different quality of fresh separator and dried separator after the spin-coating process.

2.2. Characterization

The structural information of MoO_3 was obtained with X-ray diffraction (XRD, BRUKER, D8 Focus, Germany) under the incidence angle range of 5–85°. The morphology and distribution of the MoO_3-based composite separator were characterized by scanning electron microscope (SEM, Hitachi SU8010) and transmission electron microscopy (TEM, JEM-2100). The elements of the separator and chemical states of the MoO_3 were assessed by X-ray photoelectron spectroscopy (XPS, ESCALAB 250Xi).

2.3. Electrochemical Measurements

The CR2032-type coin half-cells consist of the MoO_3-based composite separator, lithium metal and 1 M $LiPF_6$ in 1:1 (volume ratio) EC/DMC. All half-cells were assembled in a glove box and aged for about 12 hours before electrochemical measurements. The MoO_3 materials obtained by calcination from ammonium molybdate tetrahydrate were used as the control group. The MoO_3-based electrode was assembled to half-cells in the same method consistent with MoO_3-based composite separator. Performance of batteries was obtained with a battery test system (Land, China). The diffusion coefficient and capacitive contribution were determined by cyclic voltammetry (CV) tests at different scan rate (0.2 mV ∼ 1.2 mV). Electrochemical impedance spectra (EIS) were obtained from the electrochemical workstation (Zahner).

3. RESULTS AND DISCUSSION

3.1. Structure, Morphology, and Surface Characterizations

The morphology information of MoO_3-based composite separator is given in Figure 1. The active materials are successfully attached to one side of the separator (Fig. 1(a)), while the other side separator is composed of interlaced fibrous materials (Fig. 1(b)), indicating the MoO_3/CNTs successfully grown on the single side of the separator. With a simple spin-coating method, the active materials can be attached to a single side of the separator. In addition, during the spin-coating process, active materials can have a good dispersion and more active sites can be exposed. Moreover, because the area of the separator is larger than that of the current-collector, the loading capacity of the active material can be increased without too much thickness of the active material. Figure 1(c) shows that the MoO_3 materials with a particle size of ∼500 nm are interlaced with CNTs, which could improve the electrical conductivity. The Figure 1(d) shows the TEM image of MoO_3/CNTs composite materials. The MoO_3 is connected by interwoven CNTs and the interconnecting carbon tubes provide a pathway for electron transport and effectively enhance the conductivity of MoO_3 materials. The structural information of MoO_3 was obtained by XRD,

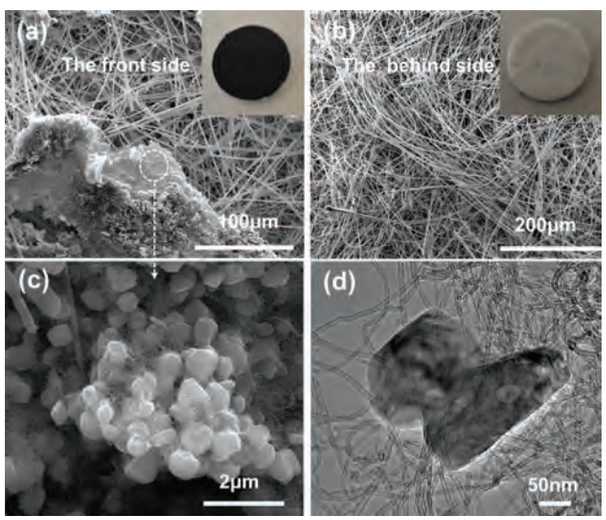

Fig. 1. SEM images and photos of MoO_3-based composite electrode: (a) (c) the front side; (b) the behind side; and (d) TEM image of MoO_3/CNTs.

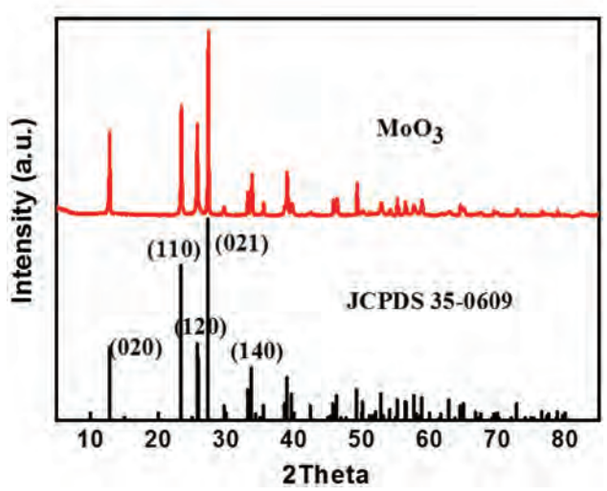

Fig. 2. The XRD pattern of MoO_3 powder sample and standard JCPDS of α-MoO_3.

as Figure 2 shows. The load of MoO_3 on the separator is too little (1∼2 mg) to detect the XRD signal. So MoO_3 powder samples (produced by calcination from ammonium molybdate) were used for XRD characterization. Its highest diffraction peak appeared in 27.3°, corresponding to the (021) crystal plane, and there are some weak diffraction peaks at 23.3°, 25.9°, 12.8°, and 34.4°, respectively corresponding to the (110), (120), (020), and (140). From the comparison of XRD experimental spectra with standard cards, the diffraction angles of the four strongest peaks corresponding to (020), (110), (120), (021) are consistent with standard cards. Their height of peaks is not exactly the same as standard cards, caused by the preferred orientation phenomenon, but that does not affect how we determine the phase structure. As for the difference between experimental data of some weak peaks and standard cards, it is due to the not exactly test results caused by the fast scanning scan speed (6°/min).The XRD results of MoO_3 are highly consistent with the PDF card (JCPDS 35-0609), indicating that the as-prepared MoO_3 is mainly composed of α-MoO_3 (Pbnm space group) [37].

Figure 3 depicts the XPS information of MoO_3-based composite separator (the front side). The Na, Si and some O elements come from the main components of the separator. Mo, O and C elements come from the MoO_3 and CNTs loaded on the separator. Weak peaks of Co and F may be caused by some impurities in the separator. The Mo3d spectra of the composite separator can be fitted into 4 peaks, as depicted in Figure 3(b). The most intense peaks at 236.29 eV and 233.15 eV corresponds to Mo^{6+} and the low intensities at 231.78 eV and 234.92 eV indicate the existence of Mo^{5+} [38]. Capacitive charge storage can occur via uptake of lithium ions by defective sides [39]. So the presence of Mo^{5+} on the surface of MoO_3 can result in a pseudocapacitive effect, improving the capacity. In addition, defects can also promote rapid ion transport [25, 40].

3.2. Electrochemical Performance

Galvanostatic charge-discharge cycling tests were performed to study the electrochemical performances of the MoO_3-based composite separator. In Figure 4(a), the cycle performance of MoO_3-based composite separator and electrode at 0.5 A g^{-1} is displayed. For the composite separator, there is an irreversible capacity on the 1st cycle, caused by some side reactions and the formation of solid electrolyte membrane. The composite separator behaves super high and continuously increasing capacity (>950 mA h g^{-1}) at the first 20 cycles, which is generally attributed to the kinetically activated electrolyte degradation with the increase of cycling number [32]. Previous literatures have also reported this common phenomenon [41, 42]. After 100 cycles discharge/charge processes, the special capacity decreases a lot, due to the structural collapse resulted by volume expansion [43] and the detachment of active substances from the separator. For the normal MoO_3-based electrode, after 100 cycles, its capacity dropped rapidly from 720 to 323 mA h g^{-1}. As Figure 4(b) shows, the discharge capacities of the MoO_3-based composite separator at 0.2, 0.5, 1, 2, 5 A g^{-1} are 1213, 1151, 980, 812, 413 mA h g^{-1}, respectively. The relative capacities of MoO_3-based electrode are 678, 580, 396, 289,

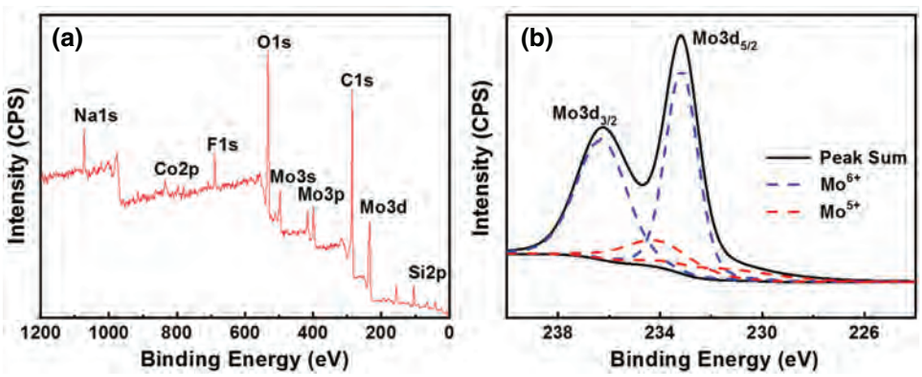

Fig. 3. XPS spectra for MoO_3-based composite separator: (a) survey spectrum; (b) Mo3d region.

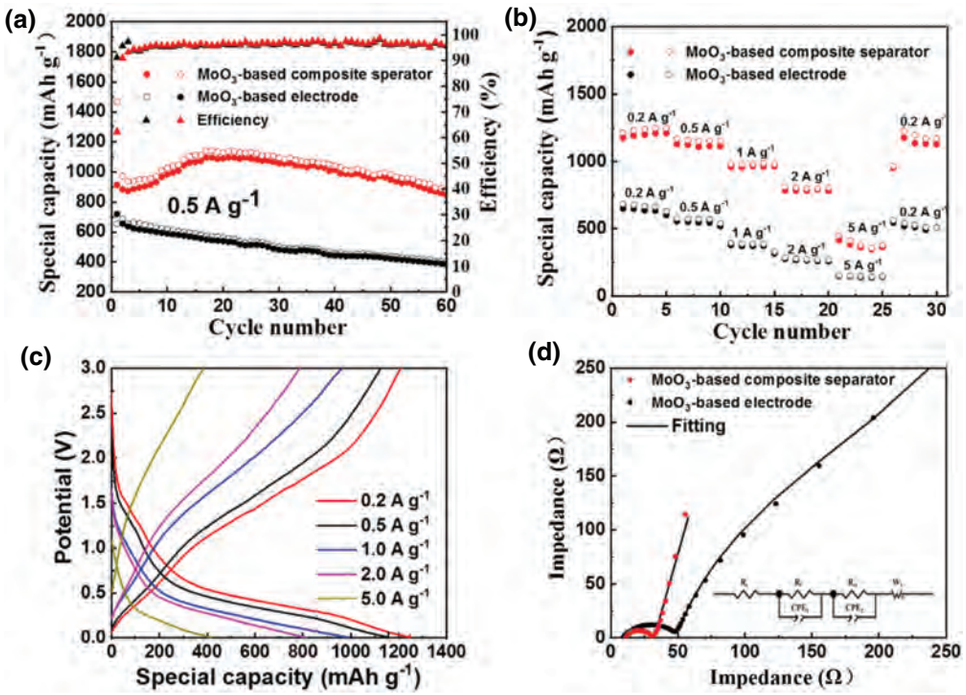

Fig. 4. (a) Cycle performance of MoO_3-based composite separator and MoO_3-based electrode under 0.5 A g^{-1}; (b) performance of MoO_3-based composite separator and MoO_3-based electrode under current density from 0.2 A g^{-1} to 5 A g^{-1}. (c) Charge-discharge curves of MoO_3-based composite separator under different current density from 0.2 A g^{-1} to 5 A g^{-1}; (d) EIS spectra of MoO_3-based composite separator and MoO_3-based electrode.

156 mA h g^{-1} respectively at 0.2, 0.5, 1, 2, and 5 A g^{-1}, lower than MoO_3-based composite separator. Two kinds of MoO_3-based half-cells both show poor stability, which is related to the fact that the large diameter of the material (~500 nm) is unable to suppress the volume expansion. Compared with the MoO_3 electrode, the composite separator has a relatively high capacity, which can be attributed to the rapid Li^+ and electron transfer brought by this structural design. The presence of vacancies may also be the reason for its high capacity because they can cause a pseudocapacitive effect.

The Figure 4(c) provides the discharge/charge voltage profiles of the MoO_3-based composite separator from 0.5 A g^{-1} to 5 A g^{-1}. The voltage plateaus at around 1.5V corresponds to the insertion of Li^+ in discharge process. A large Li^+ storage occurs in the voltage <0.5 V,which is a main reason for the high specific capacity [44]. The insertion of Li ions takes place by two steps when voltage >1.5 V and <0.7 V, respectively, as the following [45]:

$$V > 1.5 : MoO_3 + xLi^+ + xe^- \rightarrow Li_xMoO_3$$

$$V < 0.7 : Li_{xMoO_3} + yLi^+ + ye^- \rightarrow Mo + 3Li_2O$$

EIS experiments were carried out after cycles to study the effect of composite separator on R_{ct}. The raw and fitting EIS data of MoO_3-based composite separator and electrode are displayed in Figure 4(d) and the equivalent circuit model is also provided in Figure 4(d). The R_f, R_{ct}, $R_e$and W_1 in the equivalent circuit represent contact resistance, charge-transfer resistance, the sum of resistances within the bulk electrodes and Warburg resistance, respectively [46, 47]. The relative value of R_{ct} can be determined from the diameter of the semicircle in the medium-frequency region [14]. The smaller diameter of the composite separator indicates the lower charge transfer resistance. Fitting results and values of electrochemical parameters are provided in Table I. According to the fitting results of R_{ct}, the conventional MoO_3-based electrode has higher resistance than the MoO_3-based composite separator, indicating that the R_{ct} of the electrode/electrolyte interface can be effectively reduced by growing the active materials on the separator.

For further studying the ion diffusion coefficient and pseudocapacitive effect, we did the CV tests from 0.2 to 1.2 mV s^{-1}. The 1st to 5th cycle CV data at 0.2 mV s^{-1} are displayed in Figure 5(a). Li^+ are inserted into the interlayer between the MoO_6 octahedron layers and the MoO_6 octahedron intralayer at the first insertion process [48].

Table I. Impedance parameters of MoO_3-based composite separator and MoO_3-based electrode. Units: ω.

	Composite separator			Electrode		
Paraments	R_e	R_f	R_{ct}	R_e	R_f	R_ct
Value	11.03	13.52	7.75	8.77	40.10	200.50

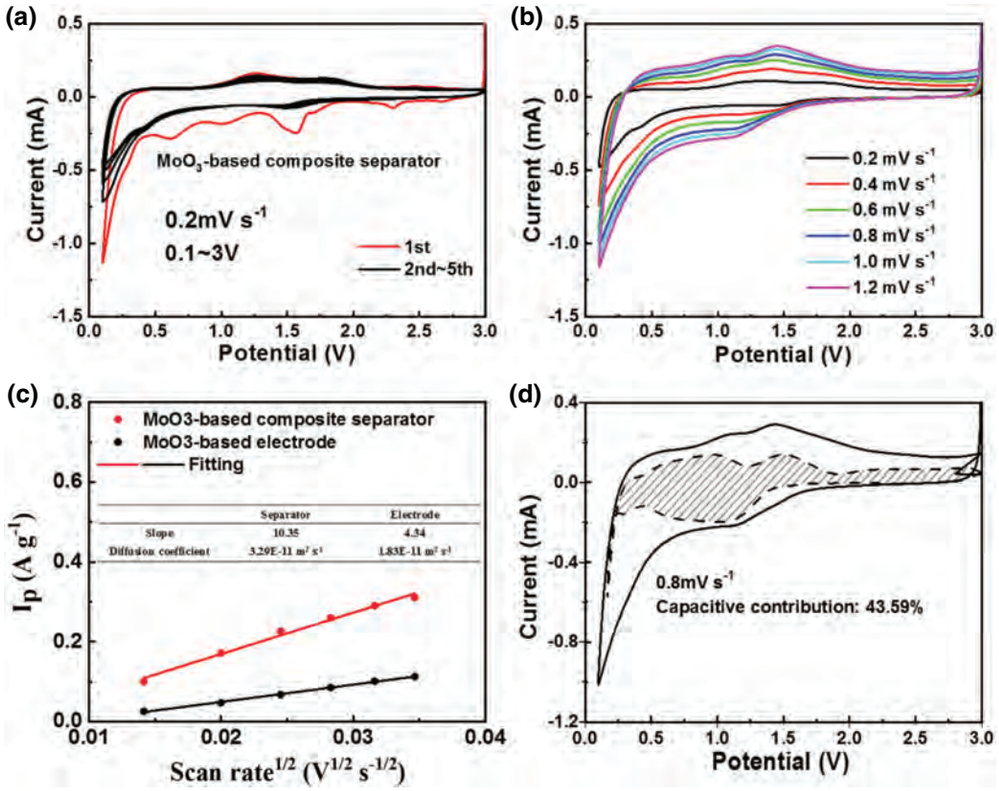

Fig. 5. (a) 1st to 5th CV curves of MoO_3-based composite separator at 0.2 mV s^{-1}; (b) CV curves of MoO_3-based composite separator at different scan rate from 0.2 mV s^{-1} to 1.2 mV s^{-1}; (c) Calculation results of the diffusion coefficient for MoO_3-based composite separator and MoO_3-based electrode; (d) Calculation results of capacitive contribution at 0.8 mV s^{-1} for MoO_3-based composite separator.

In addition, when Li^+ are inserted in Mo-O octahedron intralayer, a phase transformation of α-MoO_3 occurs, causing unrecoverable capacity [45]. In the first reduction process, peaks at around 2.2 and 2.6 V correspond to the insertion/extraction of Li^+ into the layers between the Mo-O octahedron, and the redox peak at around 1.5 V correspond to the lithium insertion reaction of α-MoO_3. These three redox peaks can all be expressed by this Eq. [45]:

$$MoO_3 + xLi^+ + xe^- \leftrightarrow Li_xMoO_3 (0 \le x \le 0.25)$$

The initial cathodic sweep exhibits a peak at 1.0 V, which is related to the intercalation of Li^+ into CNTs [49]. It should be noted that the peak at 1.0 V does not appear at following cycles, indicating that the CNTs have no contribution to capacity except for the first cycle. In the first CV curve, an irreversible peak occurs around 0.6 V, caused by some side reactions that may originate from the deposition of an organic layer on the electrode surface. [50]. These side reactions are a partial contribution to the high irreversible capacity. In the following cycles, only a pair of cathodic/anodic peaks of 1.4/1.5 V which is consistent with the discharge/charge voltage profiles can be observed, indicating irreversible capacity loss resulted from the irreversible structural transformation. Below 0.5 V, a decaying capacity can be observed, which is associated with the reaction at voltage <0.5 V. This is due to the fact that this reaction has poor reversibility [45], resulting in the poor cycle performance of MoO_3. The diffusion coefficient and capacitive contribution were estimated by CV data in Figure 5(b). The reduction peaks below 0 mA show a large shift and are not obvious, resulted by the polarization phenomenon. It is difficult to calculate the value of the diffusion coefficient corresponding to the reduction process, so only the diffusion coefficient of the oxidation peak got calculated. In Figure 5(c), we calculated the diffusion coefficient according to the following Eq. [51]:

$$\frac{I_p}{m} = (2.69 \times 10^5) \cdot C_0 \cdot A \cdot D^{1/2} \cdot v^{1/2} \quad (1)$$

The Ip, C_o, A, and represent the peak current, the initial concentration of lithium ions, the contact area, and the scan rate, respectively. For the composite separator, A is the contact area. The calculated results (Fig. 5(b)) show that the MoO_3-based composite separator has a higher diffusion rate (3.29×5310^{-11} m^2 s^{-1}), compared with the MoO_3-based electrode (1.83×5310^{-11} m^2 s^{-1}), beneficial from the novel batteries structure. The capacitive contribution was also calculated according to the Eq. (2) and (3) [52]:

$$i_d = \mathrm{nFAC} * D^{1/2} v^{1/2} \left(\frac{\alpha n F}{RT}\right)^{1/2} \pi^{1/2} \chi(bt) i_c = v C_d A \quad (2)$$

Where the i_d is the diffusion-controlled current and i_c is the capacitive current. By calculating the capacity current distribution at each voltage point, the total capacitance contribution can be obtained. The capacitive contribution results are given in the Figure 5(d). Up to 43.59%, capacitive contribution is available at 0.8 mV s^{-1}, which may be attributed to vacancies and layers between the CNTs and active MoO_3 materials [37, 39, 53]. The pseudocapacitive effect could help result in a fast charge storage and strong performance at high current density, presenting fast lithium storage and superior capacity.

Above all, the poor stability of MoO_3-based composite separator is a big limitation, duo to the detachment of active materials detached from the separator, and the intrinsic bulk expansion issue of MoO_3 is very serious, but the MoO_3-based composite separator exhibits an extra high specific capacity (~1200 mA h g^{-1} at 0.2 C). CV results and further calculation show a larger diffusion coefficient and a pseudocapacitive effect of the composite separator. The EIS results show that the composite separator has a lower R_{ct} than the normal MoO_3-based electrode. The lower R_{ct}, fast lithium ion diffusion and capacitive storage lead to the superior high capacity of the composite separator. The low R_{ct} and higher ion diffusion rate brought by this composite separator strategy is proved.

4. CONCLUSIONS

In this work, MoO_3 and CNTs were attached on the single side of the separator with a simple spin-coating method. Such a current-collector-free battery eliminates the need for metal current collectors, which also helps reduce the cost of LIBs. Compared with the active material traditionally coated on current collector, the composite separator was proved to have lower R_{ct} and higher ion transfer efficiency. The MoO_3-based composite separator behaves a good electrochemical performance, especially the high capacity. By growing the active materials on the separator, the active materials contact better with the electrolyte and more active sites will be exposed, which is more conducive to the transport of ions from the electrolyte into the active material. The greater contact area and more active sites result in the improving specific capacity and fast ion transport. Besides, that the lower charge transfer resistance gets reduced was proved by this design, which is also a reason for the improving capacity. Electrochemical calculation results show that the capacitive storage occurs in the reduced MoO_3 materials, which is also a contribution to the fast ion transport and improvement of capacity. We offered the new strategy of the composite separator that the active materials grow directly on one side of the separator surface and verified its feasibility. This new strategy may provide an idea or reference for the development in structural design of LIBs.

Acknowledgments: This work is supported partially by Natural Science Foundation of Beijing Municipality (L172036), Joint Funds of the Equipment Pre-Research and Ministry of Education (6141A020225), Par-Eu Scholars Program, Science and Technology Beijing 100 Leading Talent Training Project, China Postdoctoral Science Foundation (2018M631419), the Fundamental Research Funds for the Central Universities (2017ZZD02, 2019QN001), and the NCEPU "Double First-Class" Graduate Talent Cultivation Program.

References and Notes

1. Zhao, D., Liu, H. and Wu, X., **2019**. Bi-interface induced multi-active MCo_2O_4@MCo_2S_4@PPy (M=Ni, Zn) sandwich structure for energy storage and electrocatalysis. *Nano Energy, 57*, pp.363–370.
2. Shi, S., Li, Z., Sun, Y., Wang, B., Liu, Q., Hou, Y., Huang, S., Huang, J. and Zhao, Y., **2018**. A covalent heterostructure of monodisperse Ni_2P immobilized on N, P-co-doped carbon nanosheets for high performance sodium/lithium storage. *Nano Energy, 48*, pp.510–517.
3. Zhao, D., Wu, X. and Guo, C., **2018**. Hybrid MnO_2@$NiCo_2O_4$ nanosheets for high performance asymmetric supercapacitors. *Inorganic Chemistry Frontiers, 5*(6), pp.1378–1385.
4. Liu, H., Zhao, D., Liu, Y., Hu, P., Wu, X. and Xia, H., **2019**. Boosting energy storage and electrocatalytic performances by synergizing $CoMoO_4$@$MoZn_{22}$ core–shell structures. *Chemical Engineering Journal, 373*, pp.485–492.
5. Ma, J., Wang, D. and Sheng, P., **2018**. Iron Oxide (Fe_3O_4)–Graphene Oxide (GO) nanocomposites based li-ion batteries: Experimental and theoretical studies. *Journal of Nanoelectronics and Optoelectronics, 13*(12), pp.1886–1896.
6. Wu, X. and Yao, S., **2017**. Flexible electrode materials based on WO_3 nanotube bundles for high performance energy storage devices. *Nano Energy, 42*, pp.143–150.
7. Huang, S., Lv, Y., Tie, D., Yu, Y. and Zhao, Y., **2019**. Realizing simultaneously enhanced energy and power density full-cell construction using mixed hard carbon/$Li_4Ti_5O_{12}$ electrode. *Rare Metals*, pp.1–7.
8. Yu, Y., Huang, S., Wang, B., Tie, D., Wang, Q., Hou, Y. and Zhao, Y., **2019**. Achieving high-energy full-cell lithium-storage performance by coupling high-capacity V_2O_3 with low-potential Ni_2P Anode. *ACS Appl. Mater Interfaces, 11*(1), pp.19–25.
9. Xu, Y., **2017**. Capacity estimation and cascade utilization method of retired lithium ion batteries. *Journal of Nanoelectronics and Optoelectronics, 12*(8), pp.803–807.
10. Mahmood, N., Tang, T. and Hou, Y., **2016**. Nanostructured anode materials for lithium ion batteries: Progress, challenge and perspective. *Advanced Energy Materials, 6*(17), p.1600374.
11. Zhou, L., Zhang, K., Hu, Z., Tao, Z., Mai, L., Kang, Y.-M., Chou, S.-L. and Chen, J., **2018**. Recent developments on and prospects for electrode materials with hierarchical structures for lithium-ion batteries. *Advanced Energy Materials, 8*(6), p.1701415.
12. Li, S., Hu, B. and Zhang, F., **2017**. Investigation of chloride corrosion process of cement and concrete-based materials based on electrochemical impedance spectroscopy. *Journal of Nanoelectronics and Optoelectronics, 12*(11), pp.1244–1250.
13. Wu, M., Xu, B. and Ouyang, C., **2016**. Physics of electron and lithium-ion transport in electrode materials for Li-ion batteries. *Chinese Physics B, 25*(1).
14. Tang, C., Liu, Y., Xu, C., Zhu, J., Wei, X., Zhou, L., He, L., Yang, W. and Mai, L., **2018**. Ultrafine nickel-nanoparticle-enabled SiO_2 hierarchical hollow spheres for

high-performance lithium storage. *Advanced Functional Materials, 28*(3), p.018206.

15. Chen, Y.M., Yu, L. and Lou, X.W., **2016**. Hierarchical tubular structures composed of Co_3O_4 hollow nanoparticles and carbon nanotubes for lithium storage. *Angewandte Chemie International Edition, 55*(20), pp.5990–5993.
16. Ko, M., Chae, S., Jeong, S., Oh, P. and Cho, J., **2014**. Elastic a-silicon nanoparticle backboned graphene hybrid as a self-compacting anode for high-rate lithium ion batteries. *ACS Nano, 8*(8), pp.8591–8599.
17. Wang, Z.L., Xu, D., Wang, H.G., Wu, Z. and Zhang, X.B., **2013**. *In situ* fabrication of porous graphene electrodes for high-performance energy storage. *ACS Nano., 7*(3), pp.2422–2430.
18. Feckl, J.M., Fominykh, K., Doblinger, M., Fattakhova-Rohlfing, D. and Bein, T., **2012**. Nanoscale porous framework of lithium titanate for ultrafast lithium insertion. *Angewandte Chemie International Edition, 51*(30), pp.7459–7463.
19. Wang, L., He, X., Li, J., Sun, W., Gao, J., Guo, J. and Jiang, C., **2012**. Nano-structured phosphorus composite as high-capacity anode materials for lithium batteries. *Angewandte Chemie International Edition, 51*(36), pp.9034–9037.
20. Lee, M.J., Lee, S., Oh, P., Kim, Y. and Cho, J., **2014**. High performance $LiMn_2O_4$ cathode materials grown with epitaxial layered nanostructure for Li-ion batteries. *Nano Letter, 14*(2), pp.993–999.
21. Wang, X., Li, G., Li, J., Zhang, Y., Wook, A., Yu, A. and Chen, Z., **2016**. Structural and chemical synergistic encapsulation of polysulfides enables ultralong-life lithium–sulfur batteries. *Energy & Environmental Science, 9*(8), pp.2533–2538.
22. Huang, S., Wang, M., Jia, P., Wang, B., Zhang, J. and Zhao, Y., **2019**. N-graphene motivated SnO_2@SnS_2 heterostructure quantum dots for high performance lithium/sodium storage. *Energy Storage Materials, 20*, pp.225–233.
23. Zhao, D., Dai, M., Liu, H., Xiao, L., Wu, X. and Xia, H., **2019**. Constructing high performance hybrid battery and electrocatalyst by heterostructured $NiCo_2O_4$@NiWS nanosheets. *Crystal Growth & Design, 19*(3), pp.1921–1929.
24. Zhao, D., Hu, F., Umar, A. and Wu, X., **2018**. $NiCo_2O_4$ nanowire based flexible electrode materials for asymmetric supercapacitors. *New Journal of Chemistry, 42*(9), pp.7399–7406.
25. Wu, H., Guo, Z., Zhou, J. and Sun, Z., **2019**. Vacancy-mediated lithium adsorption and diffusion on MXene. *Applied Surface Science, 488*, pp.578–585.
26. Huang, S., Li, Z., Wang, B., Zhang, J., Peng, Z., Qi, R., Wang, J. and Zhao, Y., **2018**. N-doping and defective nanographitic domain coupled hard carbon nanoshells for high performance lithium/sodium storage. *Advanced Functional Materials, 28*(10), p.1706294.
27. Ruan, J., Yuan, T., Pang, Y., Luo, S., Peng, C., Yang, J. and Zheng, S., **2018**. Nitrogen and sulfur dual-doped carbon films as flexible free-standing anodes for Li-ion and Na-ion batteries. *Carbon, 126*, pp.9–16.
28. Jo, H., Wu, M., Choi, S., Jeon, H. and Jung, H.K., **2018**. Characterization of Ti(3+)-doped TiO_2 based composite electrode for lithium polymer secondary batteries. *Nanotechnology, 29*(44), p.445402.
29. Zhang, Y., Malyi, O.I., Tang, Y., Wei, J., Zhu, Z., Xia, H., Li, W., Guo, J., Zhou, X., Chen, Z., Persson, C. and Chen, X., **2017**. Reducing the charge carrier transport barrier in functionally layer-graded electrodes. *Angewandte Chemie International Edition, 56*(47), pp.14847–14852.
30. Ding, J., Abbas, S.A., Hanmandlu, C., Lin, L., Lai, C.-S., Wang, P.-C., Li, L.-J., Chu, C.-W. and Chang, C.-C., **2017**. Facile synthesis of carbon/MoO_3 nanocomposites as stable battery anodes. *Journal of Power Sources, 348*, pp.270–280.
31. Cao, D., Dai, Y., Xie, S., Wang, H. and Niu, C., **2018**. Pyrolytic synthesis of MoO_3 nanoplates within foam-like carbon nanoflakes for enhanced lithium ion storage. *Journal of Colloid and Interface Science, 514*, pp.686–693.
32. Tian, W., Hu, H., Wang, Y., Li, P., Liu, J., Liu, J., Wang, X., Xu, X., Li, Z., Zhao, Q., Ning, H., Wu, W. and Wu, M., **2018**. Metal-Organic frameworks mediated synthesis of one-dimensional molybdenum-based/carbon composites for enhanced lithium storage. *ACS Nano., 12*(2), pp.1990–2000.
33. Zhang, G., Xiong, T., Yan, M., He, L., Liao, X., He, C., Yin, C., Zhang, H. and Mai, L., **2018**. α-MoO_3- by plasma etching with improved capacity and stabilized structure for lithium storage. *Nano Energy, 49*, pp.555–563.
34. Liu, C., Jiang, W., Hu, F., Wu, X. and Xue, D., **2018**. Mesoporous $NiCo_2O_4$ nanoneedle arrays as supercapacitor electrode materials with excellent cycling stabilities. *Inorganic Chemistry Frontiers, 5*(4), pp.835–843.
35. Zhao, D., Xie, D., Liu, H., Hu, F. and Wu, X., **2018**. Flexible α-Fe_2O_3 nanorod electrode materials for sodium-ion batteries with excellent cycle performance. *Functional Materials Letters, 11*(06), p.1840002.
36. Wu, G., Chen, J., Guo, Y., Li, X., Luo, B., Chu, L., Han, Y., Jiang, B., Xu, L. and Li, M., **2017**. Freestanding sodium-ion batteries electrode using graphene foam coaxially integrated with TiO_2 nanosheets. *Journal of The Electrochemical Society, 164*(13), pp.A3060–A3067.
37. Kim, H.S., Cook, J.B., Lin, H., Ko, J.S., Tolbert, S.H., Ozolins, V. and Dunn, B., **2017**. Oxygen vacancies enhance pseudocapacitive charge storage properties of MoO3-x. *Nature Materials, 16*(4), pp.454–460.
38. Światowska-Mrowiecka, J., De Diesbach, S., Maurice, V., Zanna, S., Klein, L., Briand, E., Vickridge, I. and Marcus, P., **2008**. Li-Ion intercalation in thermal oxide thin films of MoO_3 as studied by XPS, RBS, and NRA. *The Journal of Physical Chemistry C, 112*(29), pp.11050–11058.
39. Qian, J., Wu, F., Ye, Y., Zhang, M., Huang, Y., Xing, Y., Qu, W., Li, L. and Chen, R., **2018**. Boosting fast sodium storage of a large-scalable carbon anode with an ultralong cycle life. *Advanced Energy Materials, 8*(16), p.1703159.
40. Yang, L., Chen, H.S., Song, W.L. and Fang, D., **2018**. Effect of defects on diffusion behaviors of lithium-ion battery electrodes: *In Situ* optical observation and simulation. *ACS Appl. Mater Interfaces, 10*(50), pp.43623–43630.
41. Hao, S., Zhang, B., Ball, S., Wu, J., Srinivasan, M. and Huang, Y., **2016**. Phase transition of hollow-porous α-Fe_2O_3 microsphere based anodes for lithium ion batteries during high rate cycling. *Journal of Materials Chemistry A, 4*(42), pp.16569–16575.
42. Fan, L., Zhang, Y., Zhang, Q., Wu, X., Cheng, J., Zhang, N., Feng, Y. and Sun, K., **2016**. Graphene aerogels with anchored sub-micrometer mulberry-like ZnO particles for high-rate and long-cycle anode materials in lithium ion batteries. *Small, 12*(37), pp.5208–5216.
43. Sun, H., Hanlon, D., Dinh, D.A., Boland, J.B., Del Rio Castillo, A.E., Di Giovanni, C., Ansaldo, A., Pellegrini, V., Coleman, J.N. and Bonaccorso, F., **2017**. Carbon nanotubes-bridged molybdenum trioxide nanosheets as high performance anode for lithium ion batteries. *2D Materials, 5*(1), p.015024.
44. Meduri, P., Clark, E., Kim, J.H., Dayalan, E., Sumanasekera, G.U. and Sunkara, M.K., **2012**. $MoO_{(3-x)}$ nanowire arrays as stable and high-capacity anodes for lithium ion batteries. *Nano Letters, 12*(4), pp.1784–1788.
45. Ahmed, B., Shahid, M., Nagaraju, D.H., Anjum, D.H., Hedhili, M.N. and Alshareef, H.N., **2015**. Surface passivation of MoO(3) nanorods by atomic layer deposition toward high rate durable li ion battery anodes. *ACS Applied Materials & Interfaces, 7*(24), pp.13154–13163.

46. Li, X., Wu, G., Liu, X., Li, W. and Li, M., **2017**. Orderly integration of porous TiO_2 (B) nanosheets into bunchy hierarchical structure for high-rate and ultralong-lifespan lithium-ion batteries. *Nano Energy, 31*, pp.1–8.

47. Li, X., Zhang, W., Cai, J., Yan, H., Cui, M., Wu, G. and Li, M., **2019**. Hierarchical nanosheets constructed by integration of bimetallic sulfides into N-Doped carbon: Enhanced diffusion kinetics and cycling stability for sodium storage. *Nano Energy, 62*, pp.239–249.

48. Li, W., Cheng, F., Tao, Z. and Chen, J., **2006**. Vapor-transportation preparation and reversible lithium intercalation/deintercalation of alpha-MoO_3 microrods. *Journal of Physical Chemistry B, 110*(1), pp.119–124.

49. Li, X., Fu, J., Sun, Y., Sun, M., Cheng, S., Chen, K., Yang, X., Lou, Q., Xu, T., Shang, Y., Xu, J., Chen, Q. and Shan, C., **2019**. Design and understanding of core/branch-structured VS_2 nanosheets@CNTs as high-performance anode materials for lithium-ion batteries. *Nanoscale, 11*(28), pp.13343–13353.

50. Xu, K., **2004**. Nonaqueous liquid electrolytes for lithium-based rechargeable batteries. *Chemical Reviews, 104*(10), pp.4303–4418.

51. Cholant, C.M., Azevedo, C.F., Caldeira, I., Balboni, R.D.C., Moura, E.A., Westphal, T.M., Pawlicka, A., Berton, M.A.C., Gomez, J.A. and Avellaneda, C.O., **2017**. Li + ions diffusion coefficient in V2O5:MoO3 Sol–Gel films. *Molecular Crystals and Liquid Crystals, 655*(1), pp.61–70.

52. Wang, J., Polleux, J., Lim, J. and Dunn, B., **2007**. Pseudocapacitive contributions to electrochemical energy storage in TiO_2(Anatase) nanoparticles. *The Journal of Physical Chemistry C, 111*(40), pp.14925–14931.

53. Bommier, C., Luo, W., Gao, W.-Y., Greaney, A., Ma, S. and Ji, X., **2014**. Predicting capacity of hard carbon anodes in sodium-ion batteries using porosity measurements. *Carbon, 76*, pp.165–174.